THE ASTROPHYSICAL JOURNAL, 515:525–541, 1999 April 20
© 1999. The American Astronomical Society. All rights reserved. Printed in U.S.A.

SELF-REGULATING GALAXY FORMATION AS AN EXPLANATION FOR THE TULLY-FISHER RELATION

D. ELIZONDO AND G. YEPES
Departamento de Física Teórica C-XI, Universidad Autónoma de Madrid, Cantoblanco 28049, Madrid, Spain
R. KATES AND V. MÜLLER
Astrophysikalisches Institut Potsdam, Potsdam, Germany
AND
A. KLYPIN
Department of Astronomy, New Mexico State University, Las Cruces, NM 88001
Received 1996 December 12; accepted 1998 December 1

ABSTRACT

Using three-dimensional hydrodynamical simulations of galaxy formation with supernova feedback and a multiphase medium, we derive theoretical relations analogous to the observed Tully-Fisher (TF) relations in various photometric bands. This paper examines the influence of self-regulation mechanisms including supernova feedback on galaxy luminosities and the TF relation in three cosmological scenarios: CDM, ΛCDM, and BSI (broken scale invariance). Technical questions such as dependence on resolution, galaxy-finding algorithms, and assignment procedure for circular velocity are critically examined. The luminosity functions in the B and K bands are quite sensitive to supernova feedback at the faint end studied here. We find that the faint end of the B-band luminosity function ($-18 \leq M_B \leq -15$) is $\alpha \approx -(1.5\text{–}1.9)$. This slope is steeper than the Stromlo–Automatic Plate Measuring Facility estimate but in rough agreement with the recent ESO Slice Project estimates. The galaxy catalogs derived from our hydrodynamic simulations lead to an acceptably small scatter in the theoretical TF relation amounting to $\Delta M = 0.2\text{–}0.4$ in the I band and increasing by 0.1 mag from the I band to the B band. Our results give strong evidence that the tightness of the TF relation cannot be attributed to supernova feedback alone. However, although eliminating supernova feedback affects the scatter only moderately ($\Delta M = 0.3\text{–}0.6$), it does influence the slope of the TF relation quite sensitively. With supernova feedback, $L \propto V_c^{3-3.5}$ (the exponent depending on the degree of feedback). Without it, $L \propto V_c^2$ as predicted by the virial theorem with constant M/L and radius independent of luminosity. The TF relation reflects the complex connection between depths of galaxy potential wells and the supply of gas for star formation. Hydrodynamic simulations provide direct information on this connection and its dependence on modeling parameters. Because of the small number of phenomenological parameters in our approach, it can serve as a useful laboratory for testing various hypotheses and gaining insight into the physics responsible for the scatter, slope, and amplitude of the TF relation.

Subject headings: galaxies: distances and redshifts — galaxies: luminosity function, mass function — galaxies: photometry — hydrodynamics — methods: numerical

1. INTRODUCTION

The tight observed correlation between luminosity (L) and rotational velocity (V) of spiral galaxies, $L \propto V^{3.5-4}$ (Tully & Fisher 1977; Pierce & Tully 1988, 1992) has proven to be one of the most useful tools in cosmology, most notably when applied to modeling of large-scale velocity fields and to the determination of the Hubble constant (see, e.g., Strauss & Willick 1995). However, the Tully-Fisher (TF) relation is essentially empirical and has not yet received a comprehensive physical explanation within our current attempts to understand the mechanisms of galaxy formation and evolution. Although some relationship between luminosity and rotational velocity would certainly be expected, since both of these quantities depend implicitly on the galaxy mass, the slope of the relation cannot be explained by simply combining the virial theorem ($v^2 \propto GM/R$) with a constant mass to luminosity assumption.

Processes determining the luminosity of dark matter halos must be an essential ingredient in any explanatory model. Hence, a key issue in understanding the origin of the TF relation is the effectiveness of star formation and its back-reaction on the galaxy formation process. A reliable theory of galaxy formation and evolution should be capable of answering the following questions: (1) why does the relation have a small scatter? (2) why are the slopes and zero points as observed? (3) what additional variables (either potentially observable or hidden) could explain the residuals?

Different galaxies have different merging histories and different gas accretion rates. These processes affect star formation rates and hence could introduce scatter into the distribution of galaxy luminosities and colors. Thus, the first question (low observed scatter) already represents a severe challenge for theory. Two mechanisms for explaining the low scatter were investigated by Eisenstein & Loeb (1996). First, one could suppose that galaxies formed prior to $z = 1$ and accreted only small amounts of material subsequently. However, neither the standard hierarchical clustering picture nor the particular simulations reported below support this hypothesis. Second, a strong feedback process could decouple the overall luminosity of spiral galaxies

from details of their formation histories. This kind of mechanism is quite plausible, because it is known that dynamical systems with nonlinear feedback can be efficient at "forgetting" initial conditions and at reducing sensitivity to some parameters.

The second question (zero point and steepness of the slope) involves details of the star formation history within developing galaxies. Therefore, any realistic model of galaxy formation intending to answer this question needs to take into account at least the main physical mechanisms influencing the rate of star formation: gasdynamics and radiative processes.

Finally, the processes responsible for the explanation of the TF relation involve variables (such as the merging and accretion history of the galaxy) that do not appear explicitly in the relation and that in this sense are "hidden" to the observer. A theoretical understanding, besides its importance as a basic scientific achievement, could offer several important practical advantages compared with a purely empirically based relation: First, corrections to the relation on the basis of available observable properties could improve the accuracy of distance determinations. Second, the existence of possible systematic biases (such as hidden dependence on environment) is controversial (Pierce & Tully 1988, 1992; Elizondo 1996; Elizondo et al. 1999). If present, environmental bias in distance determination could have important consequences for mapping the large-scale velocity field. Third, if the form of the TF relation is sensitive to the model of structure formation, the relation could also be useful in discriminating among cosmological scenarios.

The analysis of Eisenstein & Loeb (1996) shows that the low scatter of the TF relation is unlikely to have resulted from initial conditions. This conclusion suggests that some regulation or feedback mechanism(s) must be at work. Whatever mechanism operates, it must keep both the mass-luminosity relation and the mass-velocity relation tight. Nonlinear processes that introduce feedback into galaxy formation include energy input and metal enrichment due to supernova explosions as well as hydrodynamics. All of these processes would be expected to contribute significantly to self-regulation of galaxy luminosities.

Energy input by supernovae.—The theory of the interstellar medium (McKee & Ostriker 1977) implies that much of the energy of supernovae is converted to evaporation of cold clouds and thus has an important influence on subsequent star formation. The relative fraction of the energy used to evaporate clouds characterizes the degree of supernova feedback, as discussed below. In the context of galaxy formation and evolution, the feedback associated with injection of heat into the gas due to supernovae was studied by Yepes et al. (1997; YK^3) and found to have a significant self-regulating effect on the star formation history.

Metal enrichment.—During supernova explosions, metal-enriched gas is distributed over large volumes within a galaxy and may even be transported to the intergalactic medium, in the case of small halos. Metals strongly increase the subsequent cooling rate, resulting in an increased star formation rate. Observationally, metallicity gradients in galaxies provide evidence for the effectiveness of this mechanism in the central regions of galaxies.

Hydrodynamic feedback.—The transport of gas depends on pressure gradients, and thus it is particularly sensitive to the injection of large amounts of energy into the gas. Hence, in addition to the self-regulation due to cloud evaporation, there is also a strong self-regulating tendency due to gas flowing out of galaxies into lower density regions, where the cooling timescale is longer. Gas that remains outside the galaxy will not contribute to further star formation inside the galaxy, and star formation from the gas fraction that does eventually fall back in will be delayed.

All those feedback mechanisms are tightly coupled, and it remains to be seen how such inherently complex processes can interact to yield relatively simple characteristics and relationships such as the TF relation.

The TF relation has been investigated using so-called semianalytical models (Kauffmann, White, & Guiderdoni 1993 [KWG]; Cole et al. 1994 [CAFNZ]; Heyl et al. 1995 [HCFN]; Avila-Reese, Firmani, & Hernández 1998). Parameterizing the merging history, gas cooling, and star formation histories allows efficient generation of large synthetic galaxy data samples. The parameter space can then be investigated by testing the agreement with locally observed astrophysical processes. For example, semianalytical models have been used for studying the influence of different cosmological evolution rates on galaxy formation processes. As a first step in understanding the processes involved in the TF relation, these investigations provide quite a bit of useful information.

As in the YK^3 model used here, the baryonic content of a halo in semianalytic models (e.g., CAFNZ) typically consists of three components: hot gas, cold star-forming clouds, and stars. However, because gasdynamics is not explicitly simulated, the semianalytical models require various uncontrolled assumptions such as specification of the shape of a halo. Generally, the models idealize a galaxy halo as a round object with an assumed density profile (typically an isothermal profile $\rho \propto r^{-2}$) and constant gas temperature (equal to the virial temperature). An assumed density profile is of course not necessarily even close to a solution of the gasdynamical equations. For example, during large mergers, it is neither possible to fit the density by a simple spherical density profile, nor may the gas be treated as isothermal. In particular, an understanding of environmental influence on galaxy properties (Elizondo et al. 1999) requires a hydrodynamic treatment, because gas flows are neither spherically symmetric nor confined to the interior of halos.

Since dynamical modeling is not included, semianalytic models do not provide the flexibility of hydrodynamic simulations, which they often try to compensate for by involving extra fitting parameters. For example, as reported by HCFN, none of the models studied was able to reproduce the observed galaxy luminosity function and the TF relation simultaneously, even allowing the mass-to-light ratio to be a free parameter. It is possible to reconcile some of the discrepancies by neglecting star formation in halos with circular velocities greater than 500 km s^{-1}, as was done by KWG, but this prescription was criticized by HCFN because it is preferable to avoid introducing ad hoc assumptions. HCFN also discussed the uncertainties associated with the identification of rotational velocities of galaxies with those of halos. Note that in the semianalytical approaches, the gas is assumed isothermal out to the virial radius (radius of a sphere of overdensity 200), which as pointed out by HCFN may be violated. The scatter in the

TF relation was reported by CAFNZ to be about 0.5 mag at 200 km s^{-1}, similar to the observed values, but with an increase in the scatter for low-velocity halos.

Hydrodynamical simulations of galaxy formation (e.g., Katz 1992; Cen & Ostriker 1992; Navarro & White 1994; Steinmetz & Müller 1994; Yepes et al. 1995; YK[3]) offer the clear advantage of actually solving the gasdynamical equations. Hence, they can model the dynamical behavior of both the gas and the dark matter component at some level of accuracy in all conceivable situations, even when large mergers occur. Nevertheless, they also have their own problems, such as limited resolution. This problem should gradually decrease in severity as computational costs fall. A more serious problem is that physical processes occurring far below the resolution limit, such as star-gas interactions, can have important effects and must therefore be included by hand. However, despite these problems, hydrodynamical approaches are a complementary tool to investigate the complex area of galaxy formation and to gain insight into the origin of the properties of galaxies we observe.

The structure of this paper is as follows: we start with a brief review of basic methodology we have used for studying the theoretical TF relation, including the model, simulation techniques, and galaxy identification schemes. Next we describe and critically discuss the assignment of rotational velocity to the *numerical* galaxies (§ 3). The fits to the luminosity rotational velocity relation in the different color bands and their dependence on supernovae feedback are described in § 4. Section 5 is devoted to the study of the influence of numerical resolution and the galaxy-finding algorithm on our results. In § 6 we show our estimates of the faint end of luminosity functions in B and K bands and compare them with observational data. Finally, § 7 is devoted to the discussion of results and conclusions.

2. METHODS

2.1. *Physical Processes*

To study the origin of the TF relation, we have used three-dimensional gasdynamical simulations that include models for the most important physical processes in galaxy formation, as described by YK[3]: these include gasdynamics, radiative and Compton cooling, star formation, star-gas interactions in the form of a two-phase approximation for the interstellar medium, and supernovae feedback. The universe is modeled as a four-component medium consisting of dark matter, stars, "hot" or ambient gas, and cold clouds. Star formation is modeled by converting cold gas at a certain rate into discrete star particles. Each such event may be idealized as representing a small "starburst." Stellar population synthesis models for stars of solar metallicity (Bruzual & Charlot 1993) are used to derive the luminosities and colors of the galaxies as a superposition of the starburst contributions.

The equations for the multifluid dynamics including star formation and supernova feedback, effects of resolution, and the values of "chemical" parameters were reported in detail by YK[3]. Here we summarize the physical model in a slightly simplified form.

In each volume element, the amount of cold gas $m_{\rm cold}$ capable of producing stars is regulated by the mass of the hot gas $m_{\rm hot}$ that can cool on the timescale $t_{\rm cool}$, by the rate of forming new stable stars, and by the effects of supernova formation, which reheat and evaporate cold gas. The supernovae formation rate is assumed to be proportional to the mass of cold gas: $\dot{m}_{\rm SN} = \beta m_{\rm cold}/t_* \equiv m_{\rm SN}/t_*$, where $t_* = 10^8$ yr is the timescale for star formation and β is the fraction of mass of newly formed stars that explode as supernovae ($\beta = 0.12$ for the Salpeter initial mass function). Each 1 $M_\odot$ of supernovae supplies $E_{\rm SN} = 4.5 \times 10^{49}$ ergs of heat to the interstellar medium. However, some fraction of this energy is used to evaporate a mass $A_\odot$ of cold gas. The dimensionless factor A is taken as a constant and is referred to in what follows as the *supernova feedback parameter*. It turns out to be the most important parameter in the model. Large values of A imply that a relatively large fraction of the energy supplied by supernovae will be consumed in converting gas from the cold to the hot phase, leaving less energy to reheat the gas. On the contrary, low A-values imply that a large fraction of the supernovae energy is available to reheat the gas to higher temperatures, creating strong pressure gradients.

The mass transfer between different components satisfies

$$\dot{m}_{\rm hot} = \frac{A m_{\rm SN}}{t_*} - \frac{m_{\rm hot}}{t_{\rm cool}} ,$$

$$\dot{m}_{\rm cold} = -\frac{(m_{\rm cold} - m_{\rm SN})}{t_*} - \dot{m}_{\rm hot} ,$$

$$t_{\rm cool} = \frac{k T_{\rm hot}\, \mu m_{\rm H}}{\rho_{\rm hot}\, \Lambda(T_{\rm hot}) C(\gamma - 1)} , \qquad (1)$$

where k is the Boltzmann constant, $T_{\rm hot}$ is the temperature of the hot gas, μ is the molecular weight per particle, $m_{\rm H}$ is the mass of hydrogen, $\rho_{\rm hot}$ is the density of the hot gas, Λ is the cooling rate, and $\gamma = 5/3$ is the ratio of specific heats. The adjustable parameter $C = 1$–10 in the cooling time mimics the effects of unresolved substructure.

In order to incorporate the effects of metallicity into our model, we assume that the gas has solar composition in those regions where star formation has occurred. In these regions, we take the cooling rate $\Lambda(T)$ corresponding to a plasma with solar abundance and we assume $C = 10$ because there is a fully developed multiphase medium. In regions where no previous star formation has occurred, we assume primordial composition for the gas and take $\Lambda(T)$ for a plasma with primordial abundances and assume $C = 1$. Therefore, in our model, all the starbursts are formed from a gas of solar metallicity.

In the regime of active star formation, the main effects defining the temperature of the gas are supernova feedback and evaporation of the cold gas, which absorbs a significant fraction of the supernova energy:

$$m_{\rm hot}\, \dot{T}_{\rm hot} = \frac{m_{\rm SN}}{t_*} [T_{\rm SN} - A(T_{\rm hot} - T_{\rm cold})] . \qquad (2)$$

In this equation, $T_{\rm cold} \sim 10^4$ K is the temperature of the cold gas and $T_{\rm SN} = 1.1 \times 10^8$ K is a measure of the energy released by a supernova: $k T_{\rm SN} = (\gamma - 1)\mu m_{\rm H} \langle E_{\rm SN} \rangle / \langle m_{\rm SN} \rangle$. In order to mimic the effects of photoionization by quasars and AGNs, gas with overdensity less than 2 was kept at a constant temperature of $10^{3.8}$ K (Giroux & Shapiro 1986; Petitjean, Mücket, & Kates 1995). YK[3] found that results are relatively insensitive to the cooling enhancement factor C. For example, changing the factor from 1 to 10 gives practically the same results. This occurs because of the rapid increase in gas density after gravitational collapse sets in, leading to very effective cooling even for $C = 1$.

2.2. *Overview of Numerical Simulations*

The YK[3] code used here employs a combined particle-mesh (PM) N-body and hydrodynamic technique. The Eulerian hydrodynamical equations in the expanding universe are solved on a grid using the piecewise parabolic method (Colella & Woodward 1984). The method includes high-resolution shock capturing technique and is capable of resolving hydrodynamic shocks without artificial viscosity.

In what follows, all quantities are expressed in physical units in which the Hubble constant of the corresponding cosmological scenario has been included (see Table 1).

A set of 11 simulations was first performed and analyzed for each of the cosmological scenarios used. This provides sufficiently large catalogs of "numerical galaxies" to allow statistically significant comparisons with observational quantities. These simulations were run using 128^3 particles on a 128^3 grid, both for the dark matter and the gas-dynamics. We chose a box size of 5 Mpc as a compromise between the requirement of taking a representative part of the universe and having enough resolution to describe the mean star formation activity in a cell of the simulation volume. The cell size is thus 39 kpc, and the mass per particle is $\sim 4 \times 10^6\ M_\odot$. The supernova feedback parameter in this simulation set was $A = 200$.

To study the effects of numerical resolution, we ran a test simulation for ΛCDM with the same box size and chemical parameters as the 11 realizations, but with 256^3 particles and cells (i.e., 19.5 kpc comoving and $3.3 \times 10^5\ M_\odot$ mass per particle). We then reran this simulation at lower resolution (128^3 particles and cells). The initial particle distributions for all simulations were set up by the Zeldovich approximation. The displacement field used for the 128^3 grid was generated by a numerical average over the eight nearest cells of the displacement field in the 256^3 grid. This procedure allowed us to identify the same (massive) halos at the end of evolution in both simulations, which made possible a reliable comparison of the effects of resolution in the final observational properties of the halo distribution. Increasing the resolution by a factor of 2 did not result in significant changes in global parameters (mass, luminosity) of bright galaxies. In particular, no systematic change in the TF fit was found. Details and additional tests are reported in § 5.

To study the effects of supernovae feedback on the final observational properties of simulated galaxies, we repeated six of the 11 simulations for each cosmological model with the feedback parameter values $A = 50$ (strong gas reheating) and $A = \beta = 0$), i.e., no reheating or mass transfer; this case is referred to as "no supernova feedback." Note, however, that we include metallicity enrichment even in this case (see § 2.1). In what follows, when we refer to the $A = 0$ case we mean the no supernova feedback model as explained above. A detailed discussion of the effects of supernova feedback on the TF relation is given in § 4.

The numerical code is parallelized to a degree of 95% for symmetric multiprocessor computer architectures. All simulations reported here were performed in SGI Power Challenge and Origin 2000 supercomputers at the European Center for Parallelism in Barcelona (CEPBA).

2.3. *Cosmological Models*

The parameters of the cosmological scenarios studied here are summarized in Table 1: We consider a standard CDM scenario, a low-density ΛCDM scenario, and a broken-scale–invariant (BSI) scenario, which is based on a double inflation model. The BSI scenario was analyzed by Kates et al. (1995) using a PM code that included a thermodynamic model for the gas. The postrecombination power spectrum of the BSI model (for an analytic fit, see Kates et al. 1995) is similar to that of the τCDM scenario, in which the dark matter consists of a decaying neutrino.

Within the simulated range of scales, the perturbation spectra for all three scenarios follow a power law, $P(k) \propto k^{-2}$. The power spectra for the three models are shown in Figure 1. Although all three spectra are normalized to *COBE*, the spectral amplitudes differ considerably in our 5 Mpc box, because the normalization is performed on a scale much larger than the box. For example, the amplitude of the initial perturbations for BSI is about one-third

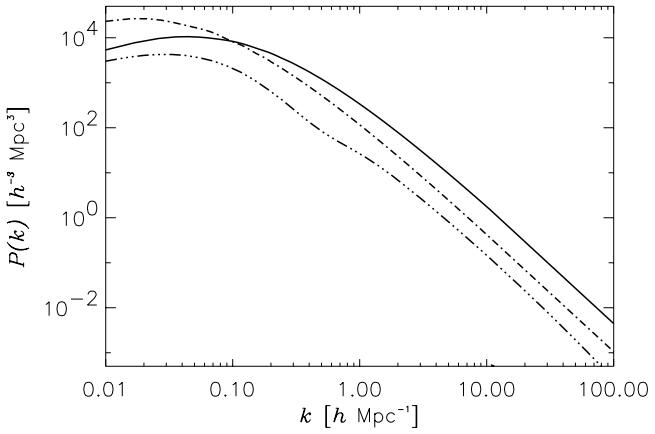


FIG. 1.—Initial power spectra for the CDM (*solid line*), ΛCDM (*dashed line*), and BSI (*dash-dotted line*) models.

TABLE 1

PARAMETERS OF THE SCENARIOS

Parameters	CDM	ΛCDM	BSI
h	0.5	0.7	0.5
Ω_Λ	0	0.65	0
Ω_B	0.051	0.026	0.051
Ω_{dm}	0.949	0.324	0.949
rms fluctuation for 8 h^{-1}Mpc (σ_8)	1.2	1.0	0.6
Simulation box at $z = 0$ (Mpc)	5	5	5
Number of particles	128^3	128^3 (256^3)	128^3
Cell size at $z = 0$ (kpc)	39	39 (19.5)	39
Mass resolution for dark matter ($10^6\ M_\odot$)	4	2.7 (0.3)	4

NOTE.—The parameters of the high-resolution simulation are in parentheses.

that of CDM. That is, our BSI simulation can be considered as a CDM simulation with an effective normalization corresponding to $\sigma_8 = 0.35$. Hence, any inferences to be drawn should not be seen as statements about the viability of scenarios, but rather as a source of information on how the merging rate (CDM vs. ΛCDM) or the time evolution (CDM vs. BSI) influences the properties of galaxies. Our references to cosmological scenario dependence in what follows are to be understood with this caveat in mind.

2.4. *Galaxy Identification Procedure*

Galaxy identification poses difficulties in cosmological N-body simulations. Here we have at our disposal a substantial piece of information that is not available in pure dark matter simulations to distinguish galaxies among dark halos: the star (luminosity) distribution. In what follows, we use the term "galaxy" to refer to a halo with nonzero luminosity.

Our halo identification algorithm was given by YK[3] and is briefly reviewed here: We begin by looking for local dark matter density maxima with overdensity greater than 100 on the grid. We then define a sphere of radius two cells centered at the position of the maxima found. The position of the center-of-mass (CM) of all particles (dark + stars) within the sphere is then computed. We then move the center of the sphere to the CM position and recompute the CM of the new particles lying within a sphere of the same radius. This procedure is iterated to convergence, which takes just a few iterations. In this way, we arrive to the true local maxima of the particle distribution. The total mass (baryons + dark matter) within the sphere is assigned as the mass for the halo. Now, if the mass within the sphere exceeds the mass corresponding to overdensity 200, we include this halo in our catalog. If the mass is lower, we repeat the algorithm with a sphere of radius one cell.

This procedure typically gives a radius and a mass for the halo that are well below the virial radius and close to the peak of the rotation curve, which is the area we are interested in. We have also checked that with this procedure, we avoid the problem of finding halos with substructures.

Using the stellar population synthesis model of Bruzual & Charlot (1993), we assign luminosities and colors to the galaxies (halos that have formed stars) by computing the spectral energy distribution (SED) according to

$$S(\lambda, t) = \sum_{\tau_i} \Phi(\tau_i) \mathscr{F}(\lambda, t - \tau_i) , \qquad (3)$$

where $\Phi(\tau_i)$ is the mass of stars in the halo produced at time step τ_i and $\mathscr{F}(\lambda, t)$ is the SED due to a starburst of 1 $M_\odot$ after an evolution time t. Convolving $S(\lambda, t)$ with the filter response function $R_f(\lambda)$, we obtain the absolute luminosity $L_f(t)$ in the given band. Combining the $L_f(t)$, we then obtain the evolution of the theoretical color index of the galaxy. (Of course, the color of a galaxy that would actually be measured will be influenced by other factors such as the interaction of starlight with the surrounding plasma.)

With this procedure, we typically obtain about a few tens of galaxy-like objects per simulation volume. In Table 2 we summarize the total number of galaxies found in all the simulations reported here. This number of galaxies permits statements concerning trends in the TF relation that are based on statistically significant estimates.

The 11 simulations carried out for each model correspond to a total simulated comoving volume of 1375 Mpc^3. Within this volume, we have also estimated the faint end of the galaxy luminosity function in the B and K bands and compare these estimates with fits to the observational data (see § 6).

In order to test the accuracy of the galaxy identification prescription, we have also used a somewhat more refined, but more computationally expensive algorithm in several of the simulations. The procedure is basically the same as above except that instead of computing quantities at fixed radius (one or two cells), we compute the spherical mass and luminosity profiles. The radius is then increased until either the overdensity in the spherical shells falls below 200 or the radius touches a neighboring halo. This procedure begins with the highest density maxima in order to define the large halos most reliably. We then define the *optical radius* (r_{opt}) of the halo, in analogy to observed galaxies, as the radius that contains $\sim 80\%$ of the total light in the B band (Persic, Salucci, & Stel 1996), assuming a pure exponential luminosity profile. The mass, circular velocity, and luminosities for the galaxies correspond to the value of their respective radial profiles at r_{opt}.

The galaxies identified by these two procedures are the same, although their physical properties deviate slightly because of the different limiting radius of the halos. Nonetheless, the main results are not substantially modified.

3. NUMERICAL ESTIMATES FOR THE ROTATIONAL VELOCITY OF GALAXIES

In observed spiral galaxies, circular disk velocities are inferred from spectroscopic line width estimates. Unfortunately, this procedure does not have a direct analog for our simulated galaxies: First, the numerical resolution of

TABLE 2

NUMBER OF GALAXIES IN THE SIMULATIONS

Model	Feedback Parameter	Number of Realizations	Number of Galaxies	Number of Bright Galaxies ($M_B < -16$)
CDM.....	$A = 200$	11	447	73
	$A = 50$	6	262	34
	$A = 0$	6	288	77
ΛCDM.....	$A = 200$	11	442	91
	$A = 50$	6	260	33
	$A = 0$	6	285	94
BSI	$A = 200$	11	649	144
	$A = 50$	6	318	36
	$A = 0$	6	317	182

our simulations (39 kpc) does not allow us to assign a morphological type by identifying a disk structure inside halos. Second, at the limits of resolution, circular velocities estimated directly from the star particles in the simulations do not provide a realistic estimate of the "true" circular velocity.

To overcome the first difficulty, we assign a morphological type for galaxies based on their colors. As it turns out, most of the galaxies in our simulations are spirals, according to their position in the UBV color diagram (see Elizondo et al. 1999 for a more detailed discussion). This result is expected, because regions with high galaxy concentrations (groups and clusters of galaxies) are underrepresented because of the limited simulation box size.

To overcome the second difficulty, we have devised an operational procedure for assigning "rotational velocities" to our numerical galaxies. We have tested this procedure for consistency in different ways. We define a gravitational (or circular) velocity, $v_{\rm grv} = \sqrt{GM/r}$, where M is the total mass (baryons + dark matter) of a galaxy within its assigned radius r of either one or two cells. To check whether our assignment of circular velocities at discrete radii is not introducing significant errors into the results, we have determined "circular velocity profiles" for a subsample of our numerical galaxies from their spherically averaged numerical density profiles. It turns out that $v_{\rm grv}$ nearly always coincides with the flat part of the rotation curve, as can be seen in Figure 2, which means that our prescription for velocity assignment is reasonably accurate.

Even for real galaxies, different observational indicators for rotation velocities can be defined, which yield different estimates of the TF relation. In a recent study, Courteau (1997) compares various measures of rotational velocity from optical rotation curves and line widths in spiral galaxies. He concludes that the best estimate of the rotation velocity for TF applications ($V_{2.2}$) is given at the location of peak rotational velocity of a pure exponential disk ($r_{\rm disk} = 2.15h$, where in this context h is the disk scale length; see, e.g., Freeman 1970). In order to check whether in the simulations our estimate of the circular velocity is compatible with the value of $V_{2.2}$, we have indicated it with an arrow in Figure 2. Assuming that the luminosity inside would follow an exponential disk profile, we can assign a characteristic disk scale length using $h = r_{\rm opt}/3.2$. The estimate of $r_{\rm opt}$ is obtained by computing the radial luminosity profiles within the halos (see § 2.4). As can be seen in the figure, the values of $V_{2.2}$ are very close (within 5%) to the values of the circular velocity assigned by our algorithm.

As another test, we constructed an estimate of the rotational velocity using the gas velocity $v_{\rm gas}$. This estimate is based on the conjecture that the hot gas well follows the depth of the potential wells confining the dark matter halos and that the gas forms a rotationally supported disk. Therefore, the temperature of the gas should provide a good indicator for the circular velocity of the gas. To construct this indicator, we take the mass-weighted average of the temperature, $\langle T\rangle_M = \int \rho_{\rm gas}\, T d^3x/M_{\rm gas}$, to estimate the gas velocity assuming an isothermal distribution, $v_{\rm gas} = \sqrt{2k\langle T\rangle_M/\mu m_p}$ (where m_p is the proton mass). The indicators $v_{\rm grv}$ and $v_{\rm gas}$ are compared for all three scenarios in Figure 3. The agreement of the two indicators is typically quite remarkable. The only outliers to the tight relation

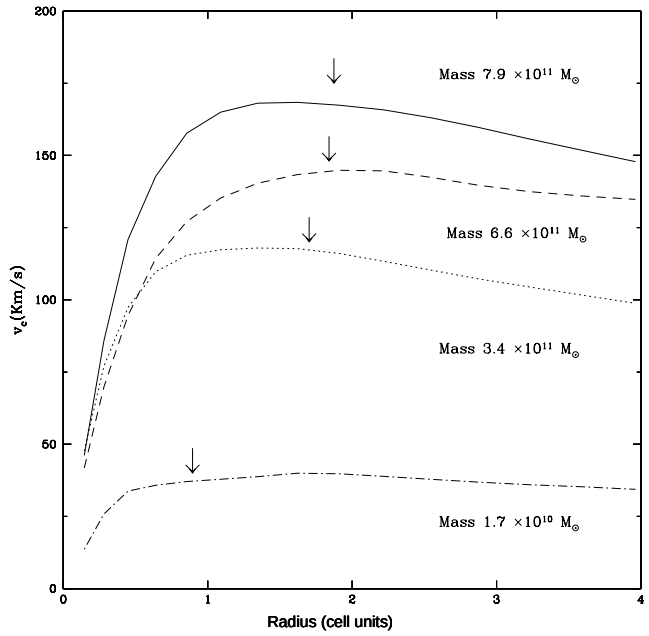


FIG. 2.—Circular velocity profiles for several halos of one of the ΛCDM simulations reported in the text. The circular velocity for the three more massive halos is assigned at two cell radii by our galaxy-finding algorithm. For the less massive halo, velocity is assigned at one-cell radii. The arrows indicate the corresponding value of $V_{2.2}$ for the different halos (see text).

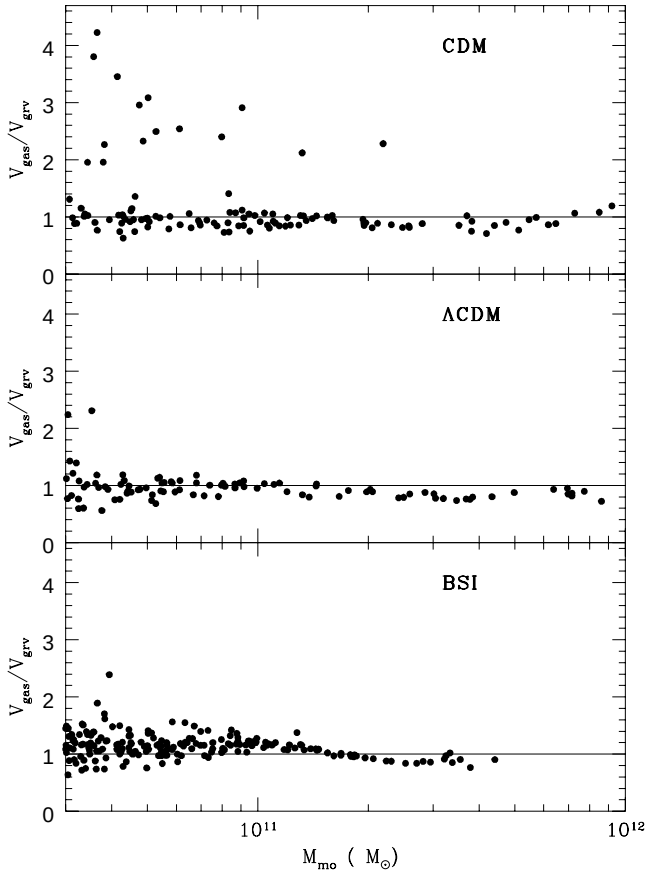


FIG. 3.—Ratio of the average gas velocity (estimated from the mass-weighted temperature) and the circular velocity of dark halos as a function of the mass of dark matter inside the halo ($M_{\rm mo}$). The points close to a ratio of 1 represent galaxies in which the gas can be considered as an isothermal sphere.

between v_{grv} and v_{gas} are located in strongly interacting satellite galaxies, where the gas temperature is strongly influenced by the environment, possibly involving increased star formation and reheating due to supernova explosions. In these cases, v_{gas} would not be expected to provide a good indicator of the circular velocity. Most of these outliers are very faint, and hence they do not contribute to the fits to the magnitude-circular velocity relation, which as explained below included only galaxies with $M_B < -16$. Exclusion of those few outliers with $M_B < -16$ from the fits has only a minor effect in the results.

Incidentally, most of the outliers arose in CDM realizations. As is plausible from the CDM spectrum (Fig. 1), the advanced stage of evolution reached in the CDM model leads to more interacting faint galaxies than in the other models.

We have also performed a further check on our assignment of rotation velocities to galaxies. High-resolution hydrodynamical simulations have found a tight correlation between baryonic mass and maximum rotation velocity of the gas, $M_{bar} \propto V_c^{2.5}$ (Evrard, Summers, & Davis 1994). On the other hand, we obtain a very tight correlation between baryonic (gas+stars) mass and total mass in our halos. Although our prescription for defining the limiting radius of our halos differs from that of Evrard et al. (1994), the mass estimates (dark and baryonic) would not differ by much. As mentioned previously, the general properties of the galaxies in our simulations do not change much when an overdensity criterion is used to define the limiting radius of halos (see § 2.4).

In Figure 4 we plot this relation for the bright ($M_B < -16$) halos found in the simulations of the three different models. The best fits to this relation give quite similar results for CDM and ΛCDM ($M_{bar} \propto M_{tot}^{1.3-1.25}$). For the less evolved BSI model, where no big galaxies have been formed up to the present epoch, we find a slightly steeper slope ($M_{bar} \propto M_{tot}^{1.45}$). We also find a tight correlation between the total mass and the gas content in the halos. In this case, the correlation is pretty much the same for the three models, $M_{gas} \propto M_{tot}^{0.6}$.

We can now use the correlation found by Evrard et al. (1994) (assuming it to be universal for dark halos in a hier-

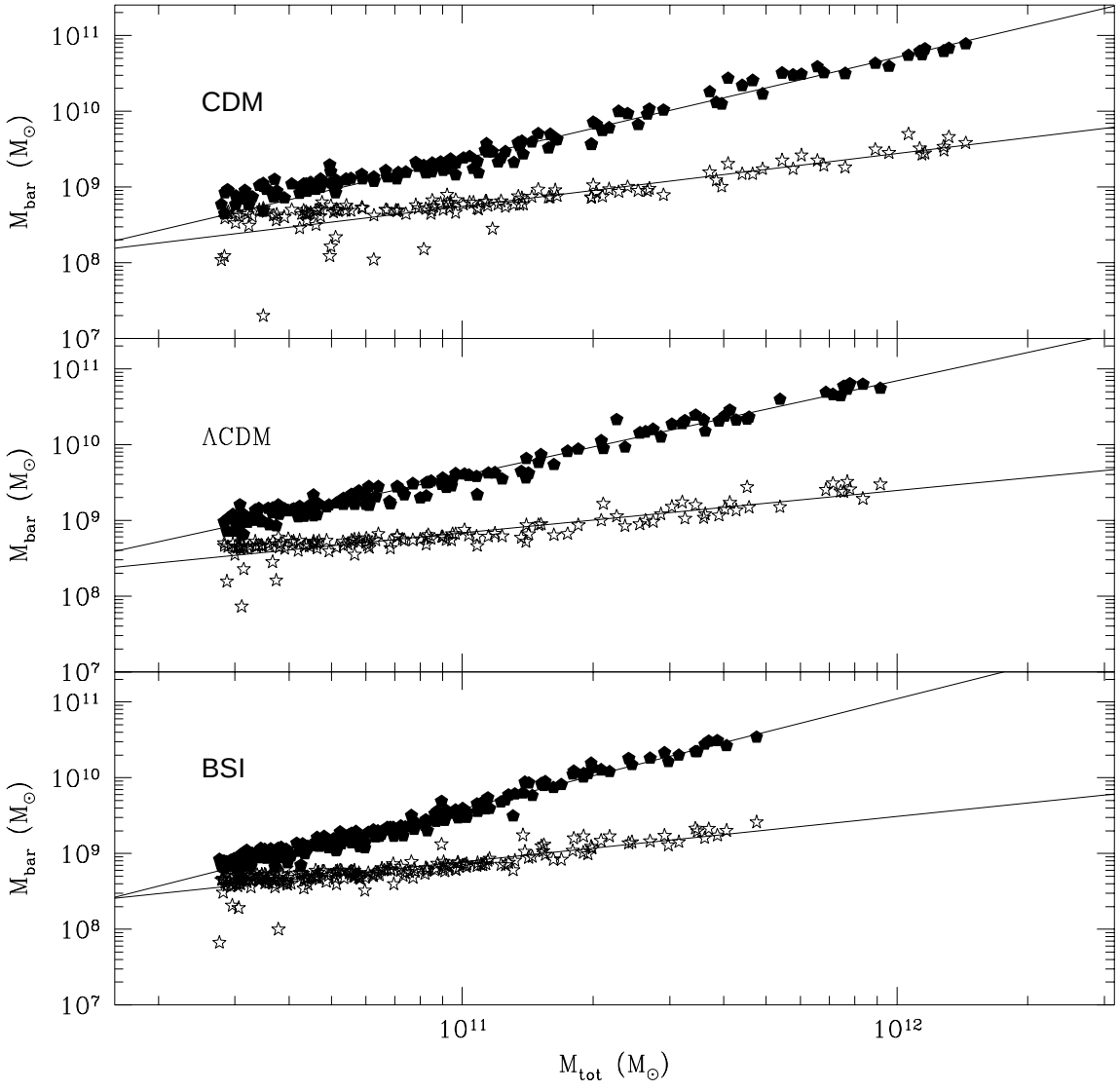


FIG. 4.—Relation between total mass and baryonic mass in the galactic halos used in the TF estimates ($M_B < -16$). Solid points represent the total mass in baryons (stars + gas), while starred symbols represent the total gas mass within the halo radius. Solid lines are the best fits to the points.

archical scenario), together with the correlation between total mass and baryonic mass found in our simulations, to obtain an independent relation between total mass and maximum circular velocity for the halos. Doing so yields $M_{\rm tot} \propto V_c^{1.8-1.9}$, which is very close to the relation we have used ($M_{\rm tot} \propto V_c^2$). Although this argument does not yield normalization constants, it provides clear evidence that at least the slope and the scatter of the TF relation computed from our simulations do not depend on the approximate procedure for estimating the circular velocity.

Further tests concerning the effects of numerical resolution and galaxy-finding algorithms on the determination of circular velocities of galaxies will be discussed in § 5.

4. FITS TO THE TF RELATION

From our galaxy samples in each scenario, we have computed magnitudes in the B, R, and I bands using the procedure of § 2.4. Figures 5, 6, and 7 are plots of the B- and I-band magnitudes versus circular velocity for the simulated galaxies in each of the three scenarios and for the three different feedback parameter values considered: $A = 200$ (realizations where the evaporation of cold clouds is the most important effect), $A = 50$ (realizations in which supernovae are very efficient at reheating the gas), and no supernova feedback (i.e., $A = \beta = 0$). All galaxies are plotted, including those with $M_B \geq -16$.

To obtain the TF relation in each band considered, we have fitted the relation between the log of the circular velocity V_c and the magnitude M in that band according to a formula of the general form

$$M - 5 \log h = a \log \left(\frac{V_c}{100 \text{ km s}^{-1}} \right) + b \qquad (4)$$

by linear least-squares regression. In order to come closer to the observational situation, the fits include only "bright" galaxies ($M_B < -16$).

Table 3 lists the resulting regression coefficients a and b and the rms scatter ΔM expressed in magnitudes in the B, R, and I spectral band for the observations (Pierce & Tully 1992) and for the simulated CDM, ΛCDM, and BSI galaxy catalogs. For each scenario, coefficients are computed for each of the supernova feedback parameters. The linear fits are also shown in Figures 5, 6, and 7.

The results shown in the table and figures illustrate the sensitivity of the TF relation to self-regulating processes affecting star formation in the halos. The different cosmological scenarios correspond to varying characteristic merging histories, while the different values of A correspond to varying supernova feedback.

Before discussing the issue of self-regulation, it is useful to point out some general trends that can be derived from the fits: Particularly noteworthy are the trends in the scatter and zero points. All models have their smallest scatter in the I band, as do observed galaxies, and in all three scenarios the B-band scatter is about 0.10 mag larger than the I-band scatter, in agreement with the observed difference. We also find the same tendency of higher (more negative) zero points for the I band than for the B band. On the other hand, we do not find a systematic increase of the TF slope toward

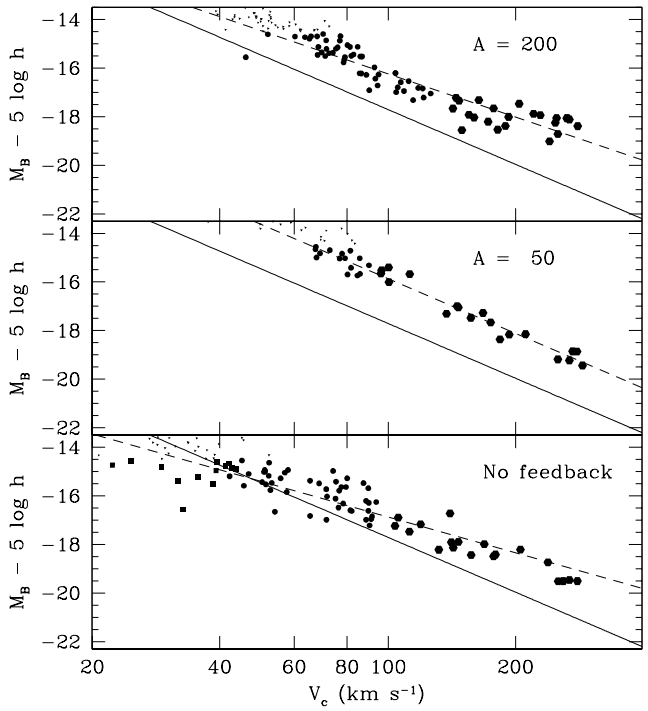


FIG. 5a

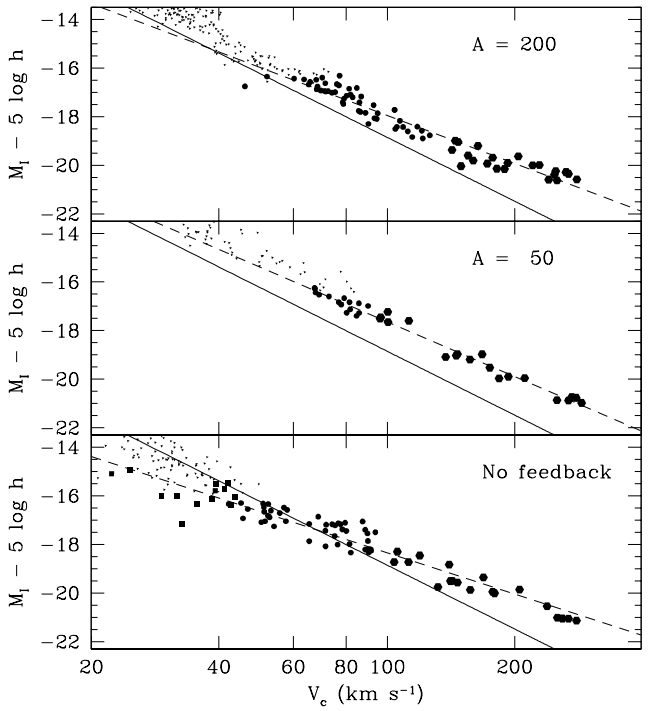


FIG. 5b

FIG. 5.—(*a*) TF relation for the B band for galaxies found in CDM simulations with different feedback parameter values. The upper panel ($A = 200$) corresponds to simulations in which evaporation of cold clouds is the most important effect. The middle panel ($A = 50$) corresponds to simulations in which supernovae are very efficient at reheating the gas but not evaporating the cold clouds. The lower panel corresponds to the same simulations run without assuming any supernova feedback process ($A = \beta = 0$ see text). Note, however, that we still kept metallicity enrichment in this case. The solid line shows the fit to the TF relation as determined by Pierce & Tully (1992). The dashed line is the best fit obtained by considering only simulated galaxies with $M_B < -16$. Filled symbols represent bright galaxies ($M_B < -16$). Hexagons represent galaxies with total mass, $M_{\rm tot} \geq 3 \times 10^{11}\ M_\odot$. Circles represent galaxies with $3 \times 10^{10}\ M_\odot < M_{\rm tot} < 3 \times 10^{11}\ M_\odot$. Squares represent galaxies with $M_{\rm tot} \leq 3 \times 10^{10}\ M_\odot$. Small crosses represent the faint galaxies ($M_B \geq -16$) found by our galaxy-finding algorithm that were not taken into account in the fit. (*b*) Same as Fig. 5*a*, but for the I band.

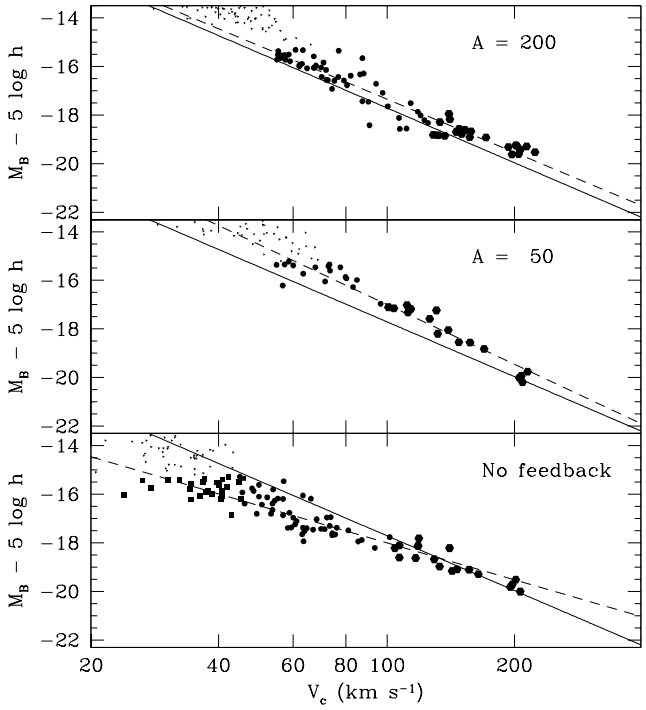


FIG. 6*a*

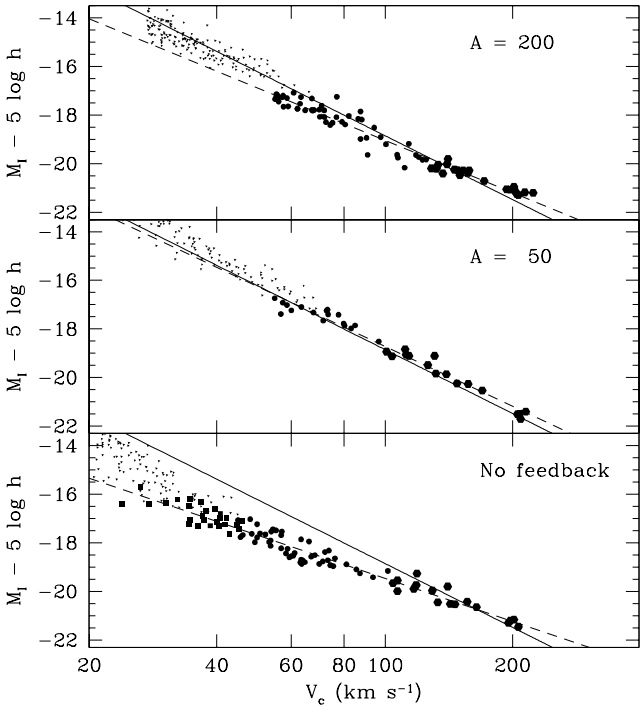


FIG. 6*b*

FIG. 6.—(*a*) Same as Fig. 5*a*, but for the ΛCDM model. (*b*) Same as Fig. 5*b*, but for the ΛCDM model.

longer wavelengths, at least when feedback from supernovae is switched on. In all models, faint galaxies ($M_B \geq -16$) seem to be systematically dimmer than predicted by the TF fit for their rotational velocities. This is consistent with results from semianalytic models (see, e.g., CAFNZ; HCFN), although in these models, the departure from linearity is more pronounced for halos with $V_c \leq 150$ km s^{-1} than in our simulations.

Concerning the effects of different cosmological scenarios, one sees that the slope of the TF relation is steeper (i.e., more negative) for less evolved models (ΛCDM and BSI). In the CDM model, galaxies with high circular velocity have a lower luminosity than that predicted from the observed TF relation. An explanation for this trend is that in the CDM

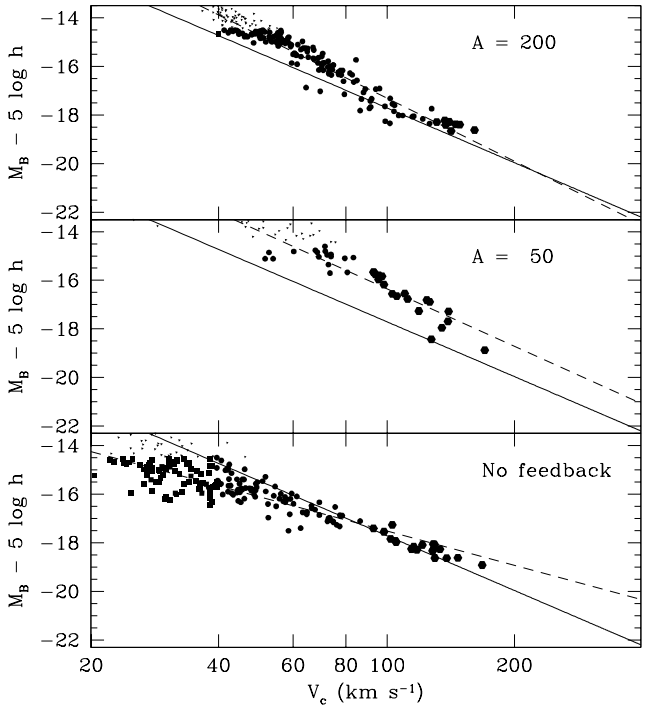


FIG. 7*a*

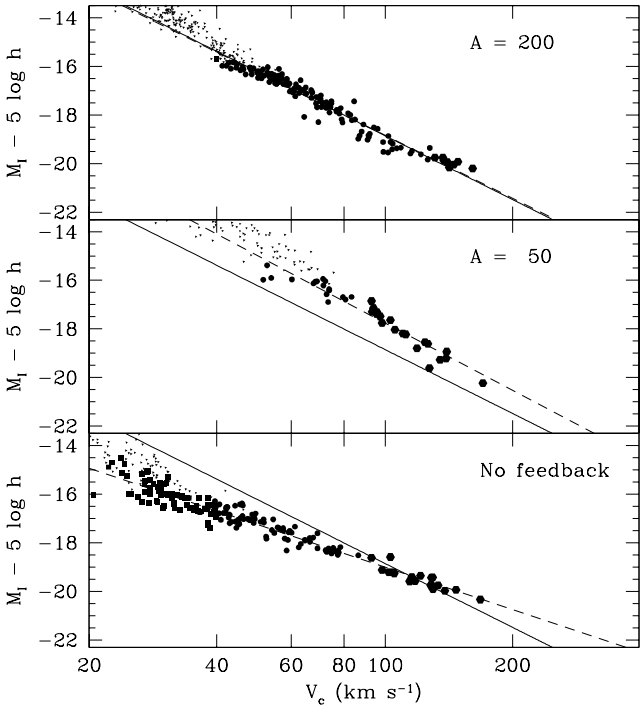


FIG. 7*b*

FIG. 7.—(*a*) Same as Fig. 5*a*, but for BSI model. Same as Fig. 5*b*, but for BSI model.

TABLE 3

PARAMETERS OF LINEAR FITS (a, b) AND SCATTER (ΔM) FOR THE MAGNITUDE–CIRCULAR VELOCITY RELATION IN DIFFERENT BANDS AND MODELS[a]

		a			b			ΔM		
MODEL	FEEDBACK PARAMETER	B	R	I	B	R	I	B	R	I
Observations.....	...	−7.48	−8.23	−8.72	−17.71	−18.47	−18.85	0.34	0.24	0.24
CDM	$A = 200$	−6.08	−6.60	−6.56	−16.21	−17.35	−16.24	0.46	0.35	0.36
	$A = 50$	−7.47	−7.49	−7.49	−15.87	−17.04	−17.63	0.29	0.22	0.21
	$A = 0$	−4.88	−5.47	−5.65	−16.87	−17.81	−18.34	0.59	0.45	0.42
ΛCDM	$A = 200$	−7.28	−7.12	−7.14	−17.68	−18.75	−19.04	0.41	0.33	0.30
	$A = 50$	−8.17	−8.18	−8.18	−16.99	−18.14	−18.72	0.39	0.27	0.25
	$A = 0$	−5.05	−5.65	−5.89	−17.99	−18.92	−19.46	0.48	0.33	0.31
BSI.....	$A = 200$	−8.60	−8.59	−8.59	−17.31	−18.29	−18.84	0.37	0.28	0.27
	$A = 50$	−7.86	−8.90	−9.20	−16.35	−17.23	−17.75	0.47	0.36	0.33
	$A = 0$	−4.67	−5.48	−5.80	−17.52	−18.44	−18.99	0.45	0.32	0.32

[a] Fits to the observational Tully-Fisher relation (Pierce & Tully 1992) are also shown.

scenario, galaxies tend to have large star formation rates at relatively early epochs. As a result, these galaxies have already transformed most of their gas into stars and the remaining gas does not cool fast enough to support a constant SFR, because it is too hot and the density is too low. The net result is a decline in the SFR of these galaxies from $z \lesssim 0.5$ up to the present epoch. A more detailed treatment is given by Elizondo et al. (1999).

Table 3 and the figures show that the slope of the TF relation depends quite strongly on the strength of supernova feedback. For low values of A (i.e., efficient gas reheating and less evaporation of cold clouds), pressure gradients are effective in driving the gas away from the center of halos with low circular velocity (≤ 150 km s^{-1}). This results in a decrease in the star formation rate and hence in fainter galaxies. On the other hand, halos with high circular velocity are hardly affected by supernovae feedback, because high-density gas efficiently radiates the energy released by supernova explosions, keeping pressure gradients low. In this regard, our simulations are in good agreement with previous work (Katz, Hernquist, & Weinberg 1992; Navarro & White 1994).

Therefore, the TF relation is steeper (more negative slope) for simulations with lower A-values. For $A = 200$, the more evolved the scenario (CDM vs. ΛCDM and BSI), the less steep the TF relation. A possible explanation is that in evolved scenarios, smaller halos tend to merge after having consumed most of their gas, so that there is a shift toward higher circular velocities without a corresponding increase in luminosity.

A very interesting result concerns the scatter of the TF relation in simulations with $A = \beta = 0$ (no heating or evaporation, but with metal enrichment). ΔM is higher than for simulations with feedback. Nevertheless, it is still comparable to the observational estimates. This seems to imply that the origin of the small scatter in the TF relation cannot be attributed solely to nonlinear feedback processes from supernova explosions. We will discuss this point in § 7. The slope of the TF relation for $A = 0$ is quite similar in all three cosmological models. It is flatter than in simulations with feedback and very different from the observations. However, the luminosities of large circular velocity halos are not strongly affected by turning off feedback.

5. NUMERICAL EFFECTS

Previous tests of our numerical simulation code were reported by YK[3]. For the present study, several additional controls and tests were carried out to quantify the effects of numerical resolution on our results. As explained in § 2.1, one of the ΛCDM realizations was simulated at two different resolutions. We can thus study the sensitivity of both the circular velocity estimate and the magnitude assignment to numerical resolution and check for biasing in the slope of the TF relations in different bands.

Figure 8 shows the circular velocity profiles as a function of radius for the four most massive halos found in the test simulation. The circular velocity estimates at the limiting radius for these halos differ by less than 10% despite the factor of 2 difference in cell width.

In Figure 9, we plot magnitudes versus circular velocities in the B and R bands for the galaxies found in the simulation with 256^3 particles and cells (19.5 kpc resolution, *solid dots*) and in the 128^3 simulation (39 kpc resolution, *asterisks*). The effects of resolution on magnitude are more pronounced for low circular velocity halos than for high circular velocity halos. Nonetheless the linear fit to the relation is hardly affected.

In the high-resolution simulation, we find that ΔM_B is reduced by $\sim 20\%$ and ΔM_R by $\sim 30\%$ as compared with the results for the low-resolution simulation. From this analysis, we conclude that our star-gas model results in galaxies with properties that are robust with respect to a factor of 2 change in numerical resolution.

As an independent test of the effects of resolution on the circular velocity profiles of dark halos, one of the CDM realizations was also simulated using the Adaptive Refinement Tree (ART) N-body code of Kravtsov, Klypin, & Khokhlov (1997). The formal resolution of this simulation, at $z = 0$ is ~ 0.2 kpc. Despite the relatively low resolution of our simulation, the overall structures of dark halos are similar to those of the ART simulation. We have identified the most massive dark halos and computed the velocity profiles, for dark matter only, in both simulations. In Figure 10 we show the results of this comparison for four typical massive halos. As expected, the differences are striking at scales smaller than our cell resolution (39 kpc). However, at

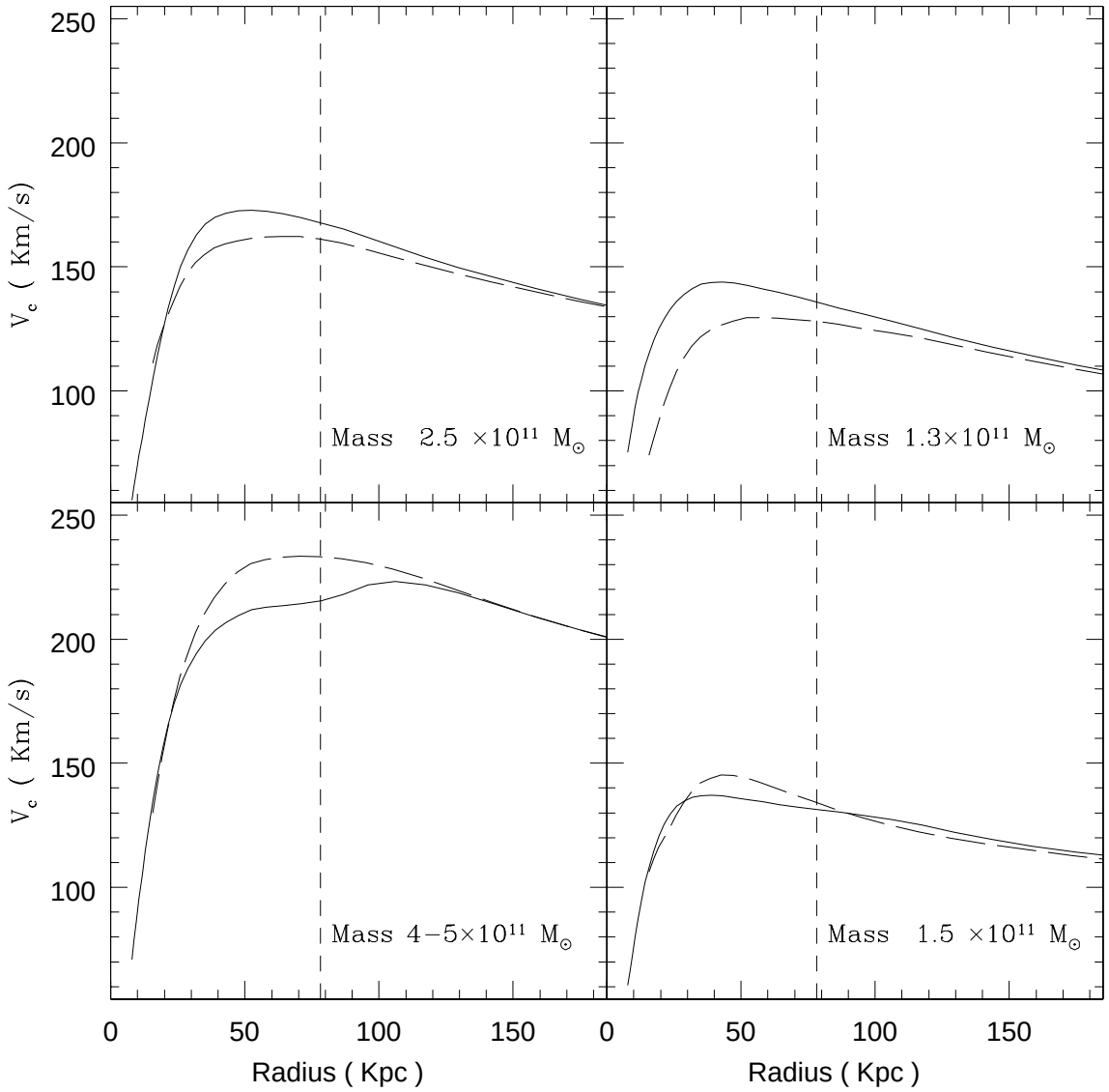


FIG. 8.—Effects of resolution on the circular velocity profile of four more massive halos in one of the ΛCDM simulations reported in the paper. The solid line is the circular velocity for the high-resolution simulation (256^3). Dashed lines correspond to the halos found in the same realization that was rerun at lower resolution (128^3). The vertical dotted line represents the limiting radius for these halos according to our galaxy-finding algorithm.

the two-cell radius, our circular velocity estimate coincides almost exactly with the high-resolution estimate. The peak of the velocity curve of halos found in the ART simulation is up to a factor of ~ 2 larger than the maximum of the velocity profile from our simulation. Nevertheless, circular velocities are assigned at the two-cell radius, not at the peak, and luminosities are also defined within the two-cell radius for massive galaxies.

6. LUMINOSITY FUNCTIONS

Semianalytical models of galaxy formation have found it very difficult to reconcile the observed zero point of the TF relation with the overall amplitude of the luminosity function (LF). It has been argued (Frenk et al. 1997) that this problem is related to the overabundance of dark matter halos predicted in all CDM cosmologies. Dark matter simulations indicate that the mass function of galactic halos has a slope of $\alpha \sim -2$ at the low-mass end, which is steeper than any estimate of the observed field galaxy LF. Hydrodynamical simulations such as those reported in this paper and semianalytical models (i.e., CAFNZ) have demonstrated that the faint end of the LF is very sensitive to the combined effects of mergers and supernova feedback.

In Figures 11 and 12 we show the LFs (*solid circles*) in the B and K bands estimated from the numerical galaxies generated in the realizations of the three cosmological simulations with different feedback parameters (*top panels*: $A = 200$; *central panels*: $A = 50$; *bottom panels*: no feedback). Observational estimates for the local LFs are also shown. For the B band, the solid line represents the Schechter function with $\alpha \sim -1$, which best fits the observational data from the Stromlo–Automatic Plate Measuring Facility (APM) survey (Loveday et al. 1992). The dashed line shows a more recent estimate of the LF found from the ESO Slice Project (ESP) galaxy redshift survey by Zucca et al. (1997). These authors find a Schechter function with $\alpha = -1.22$ as an acceptable representation of the LF over the entire range of magnitudes $M_B - 5 \log h \leq -12.2$. However, their data also suggest the presence of a steepening of the LF for $M_B - 5 \log h \geq -16.8$. Such a

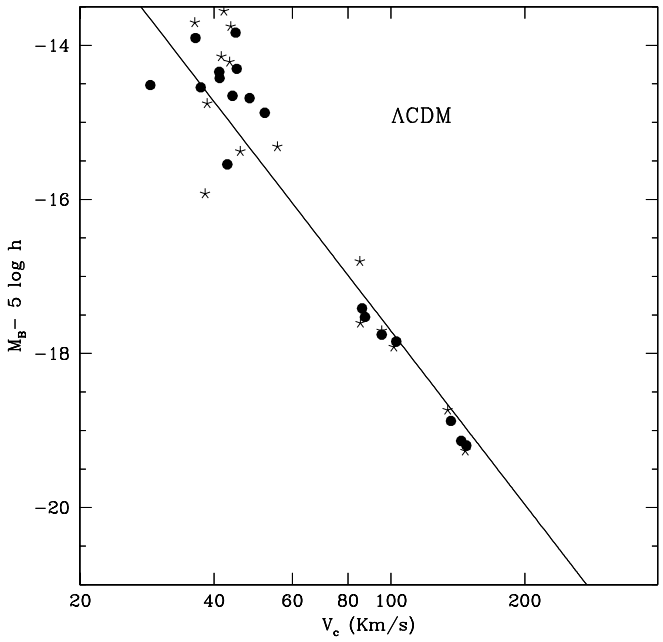


FIG. 9*a*

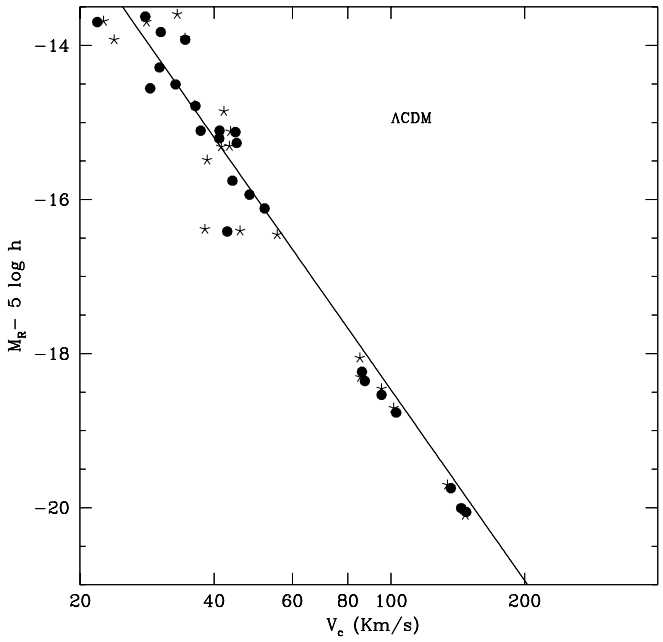


FIG. 9*b*

FIG. 9.—Effects of resolution on the TF relation (in B and R bands) for one of the ΛCDM simulations reported in this paper ($Z = 0$). The solid dots represent galaxies found in the 256^3 simulation (19.5 kpc resolution). Star points are galaxies found in the same simulation but run with 128^2 cells (39 kpc resolution) and particles. The solid line represents the observational fit to the TF relation (Pierce & Tully 1992).

steepening at the faint end of the LF is well fitted by a power law with slope ~ -1.6. The range of magnitudes of the galaxies in our simulations ($-20 \lesssim M_B \lesssim -15$) allows us to study the faint-end slope of the LF only.

In the K-band plots, we show the Schechter functions fitting the most recent observational data in the near-infrared band. Solid lines represent the best fit to the Szokoly et al. (1998) survey ($\alpha = -1.27$). Dotted lines are the best fit to the LF obtained by Gardner et al. (1997) ($\alpha = -1.03$). The dashed line corresponds to the best-fit LF obtained by Glazebrook et al. (1995) ($\alpha = -1.04$).

The lack of bright galaxies, because of the small simulated box, precludes drawing conclusions about the observed break at the bright end of the LF. The faint-end slopes of the B-band LF derived from our data are steeper ($\alpha \sim -1.5$ to -1.9, for $-18 \leq M_B \leq -15$) than the estimate of Loveday et al. (1992), but they are in rough agreement with the recent estimates from the ESP survey.

For the K band, our galaxies have magnitudes much fainter ($-22 \lesssim M_K \lesssim -14$) than those of the near-infrared redshift surveys ($M_K \lesssim -21$). Therefore, our data should be compared with the extrapolation of the best-fitting Schechter functions toward fainter magnitudes. Our data show a clear trend toward a steepening of the slope of the LF at the faint end, in agreement with the recent estimates of Szokoly et al. (1998), as compared with the results of Glazebrook et al. (1995) and Gardner et al. (1997). The slopes for the faint end of the LF from our data are in the range $\alpha \sim -1.2$ to -1.5.

In view of the dependence of the LF normalization on merging rates and supernova feedback we can explain the higher faint-end BSI LF as follows: In the BSI simulations, galaxies tend to form later than in the ΛCDM or CDM simulations. When supernova feedback is included, it most strongly affects star formation in small galactic halos, which end up fainter, as noted above. The net result is a lower normalization of the LFs for BSI with supernova feedback than without it. Efficient reheating of gas from supernovae (low A) results in an LF with lower normalization than with more evaporation (high A). Again this effect is more pronounced in the BSI simulations, because most of the galactic halos have small potential wells, so gas can more easily escape because of the relatively large pressure gradients generated by supernova explosions.

7. DISCUSSION AND CONCLUSIONS

Using hydrodynamical simulations of galaxy formation with star formation and supernova feedback we have found that it is possible to reproduce the slope, offset, and scatter of the TF relation. It is quite intriguing to ask which elements of the approach are essential for the different parts of the relation: In simulations without supernova feedback (energy input and mass transfer from supernova is switched off, but metal enrichment is left on), the slope of the resulting TF relation is too shallow, $a \sim -5$ or $L \propto V_c^2$, with nearly equal zero point in all three scenarios (cf. Table 3). This slope agrees with estimates from the Press-Schechter theory (Cole & Kaiser 1989) that incorporate cooling but ignore feedback and assume that all cold gas is converted into stars.

According to our results, the slope of the TF relation depends quite strongly on the level of feedback. The effects of supernova feedback are certainly much less significant for galaxies with $V_c \gtrsim 150$ km s^{-1} (cf. Figs. 5–7) in fairly good agreement with previous results (e.g., Navarro & White 1994; Katz, Weinberg, & Hernquist 1996).

Supernova feedback tends to have a stronger effect on star formation in low circular velocity halos. Hence supernova feedback causes a steepening of the slope, because low-mass halos become fainter while the luminosity of massive halos remains basically unchanged. This feature of

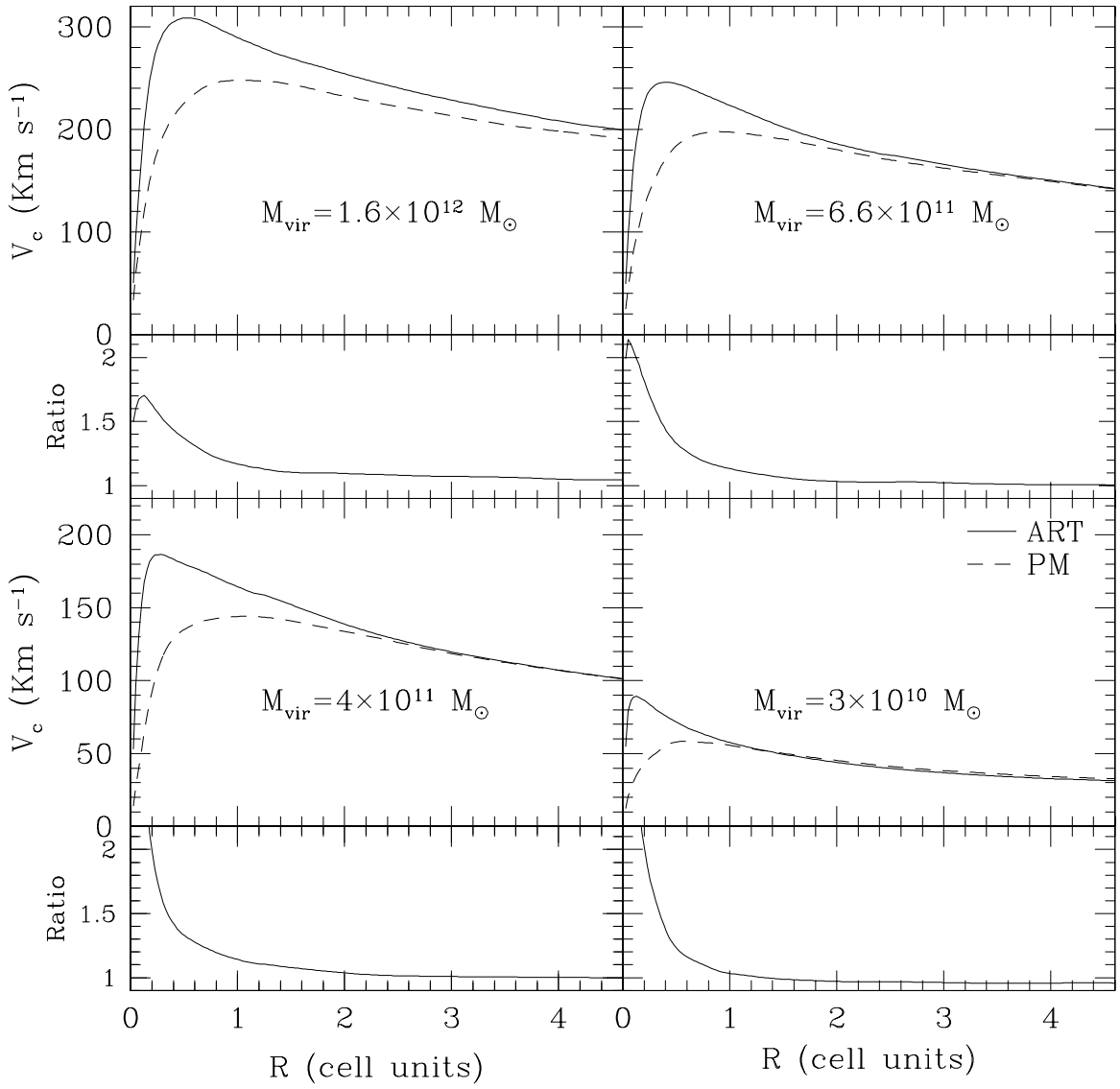


FIG. 10.—Circular velocity profiles as a function of radius (cell units of 39 kpc) for four halos found in a CDM realization simulated using two different N-body codes: a high-resolution ($\sim$0.2 kpc) ART code (Kravtsov et al. 1997) (*solid lines*) and our PM N-body code (*dashed lines*). Lower boxes in each panel show the ratio of the two circular velocity estimates as a function of radius.

the TF relation is common to the three cosmological scenarios considered here.

The slope of the TF relation is essentially the same for all photometric bands when strong feedback ($A = 50$) is considered in the more evolved models (CDM and ΛCDM), while in the less evolved scenario (BSI), the TF slope is independent of passband when moderate feedback is assumed ($A = 200$). In simulations without feedback ($A = \beta = 0$), the TF slope is steeper for redder wavelengths in all models. Although corrections for dust extinction have been made in the analysis of observations (Pierce & Tully 1992), these corrections are rather difficult to estimate and hence uncertain. The differences between the B-band and I-band TF slopes could well be attributable to dust extinction, rather than to the different star formation histories of galaxies. Moreover, recent semianalytical models that include dust extinction also find a varying slope of the TF with wavelength (Somerville & Primack 1998; Firmani & Avila-Reese 1998). In our case, we obtain an independent of passband TF slope by means of strong feedback from supernovae rather than by dust. An important extension of the present framework will be to incorporate the effects of dust extinction including a refined model for the metal production of stars.

Another important ingredient of the TF relation is the intrinsic scatter. As we have already mentioned, a long-standing question concerns whether this scatter is a consequence of cosmological conditions or whether it is rather produced by the nonlinear physical processes associated with star formation that occur in the interior of halos. Interestingly, the TF scatter does not change much as the supernova feedback parameter is varied, as long as feedback is not turned off completely (all supernova energy radiated away immediately).

However, the scatter in simulations with feedback turned off ($A = \beta = 0$) is always larger than the scatter in simulations with feedback and larger than the observed TF scatter. Feedback processes tend to reduce this scatter,

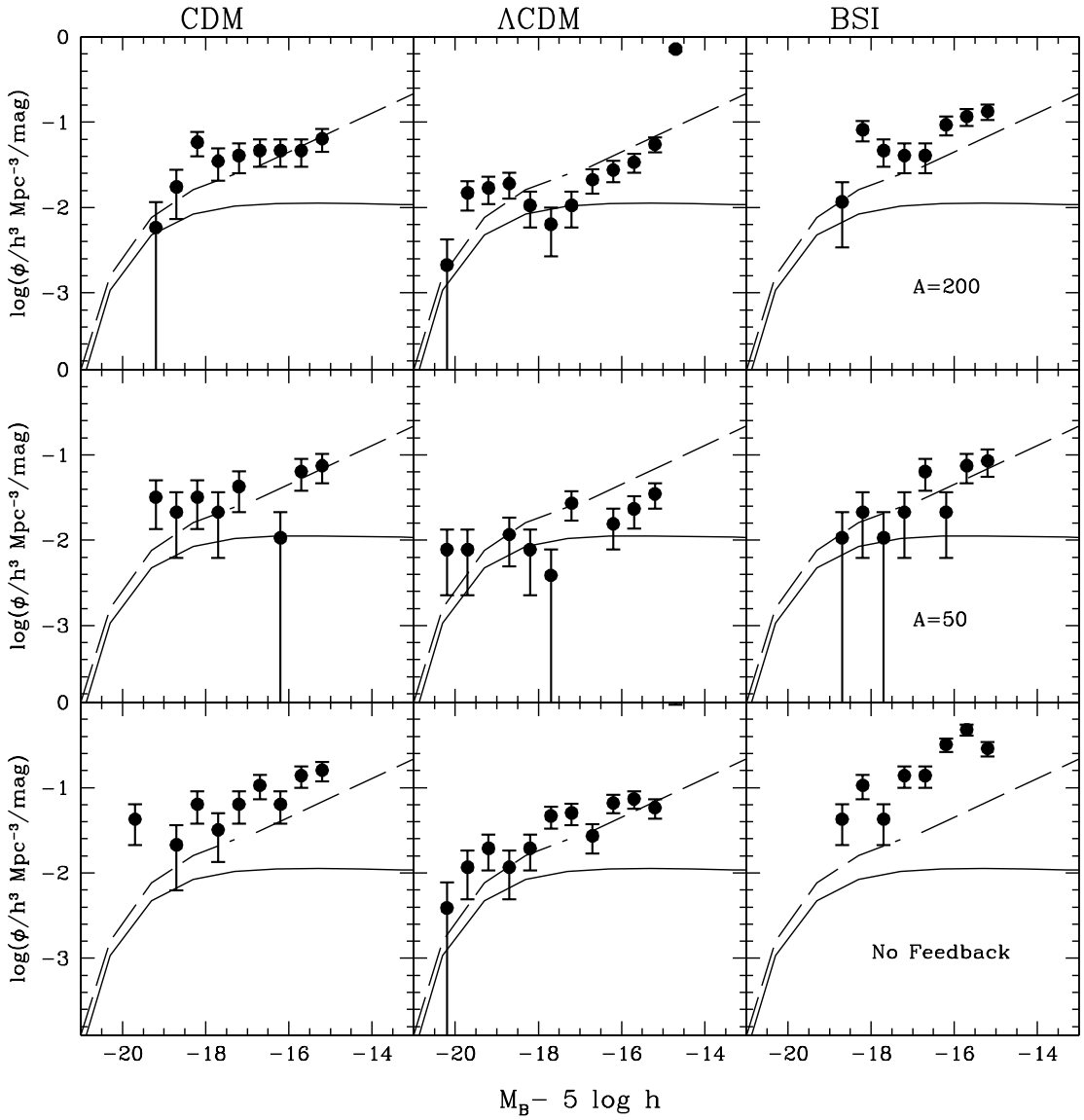


FIG. 11.—LF in the B band. Filled circles represent the LF obtained from the numerical galaxies generated in simulations with different feedback parameters (*top panels*: $A = 200$; *central panels*: $A = 50$; *bottom panels*: no feedback $A = \beta = 0$). Error bars represent Poisson errors in each magnitude bin. Solid lines are the best-fitting Schechter function from the Stromlo-APM survey (Loveday et al. 1992). The dashed line corresponds to the best fit to the LF obtained from ESP galaxy redshift survey (Zucca et al. 1997).

because they are coupled to merging rates and dynamical evolution. For instance, the rms scatter in BSI simulations is hardly affected by feedback, while in CDM simulations, the rms scatter with feedback is half that of simulations without feedback. Hence, the idea of Eisenstein & Loeb (1996) that small TF scatter is related to nonlinear feedback mechanisms could indeed be correct, but some nonlinear element in addition to supernova feedback must play an essential role in reducing it.

In a recent paper Somerville & Primack (1998) have carefully compared different semianalytical model predictions for the TF scatter and slope. They conclude that the predictions are sensitive to different assumptions concerning supernovae feedback. In particular, the "Durham semianalytical model" (CAFNZ) has a feedback model that is too strong, resulting in a nonlinear TF relation at low circular velocities. The "Munich model" (KWG) has a milder feedback model, and, consequently, it gets a flatter slope for the TF, in agreement with our numerical results. Avila-Reese et al. (1998) use a different semianalytical approach for the virialization of baryonic material in rather isolated (mass accretion dominates over major mergers) dark matter halos, without gas outflow from the disk. They find a scatter in the TF relation that is somewhat higher (within a factor of 2) than in observations (Pierce & Tully 1992), in fair agreement with what we find in our simulations with no feedback. In these semianalytical models, the scatter in the TF relation can be traced back to the scatter in the mass accretion histories of halos of similar mass (e.g., Avila-Reese 1998).

In this regard, it is interesting to compare the redshift evolution of the star formation rate for some of our halos with predictions of semianalytical calculations, kindly provided by V. Avila-Reese. In Figure 13 we show the star formation rate (SFR) as a function of redshift for three halos of different mass in one of our ΛCDM simulations. The

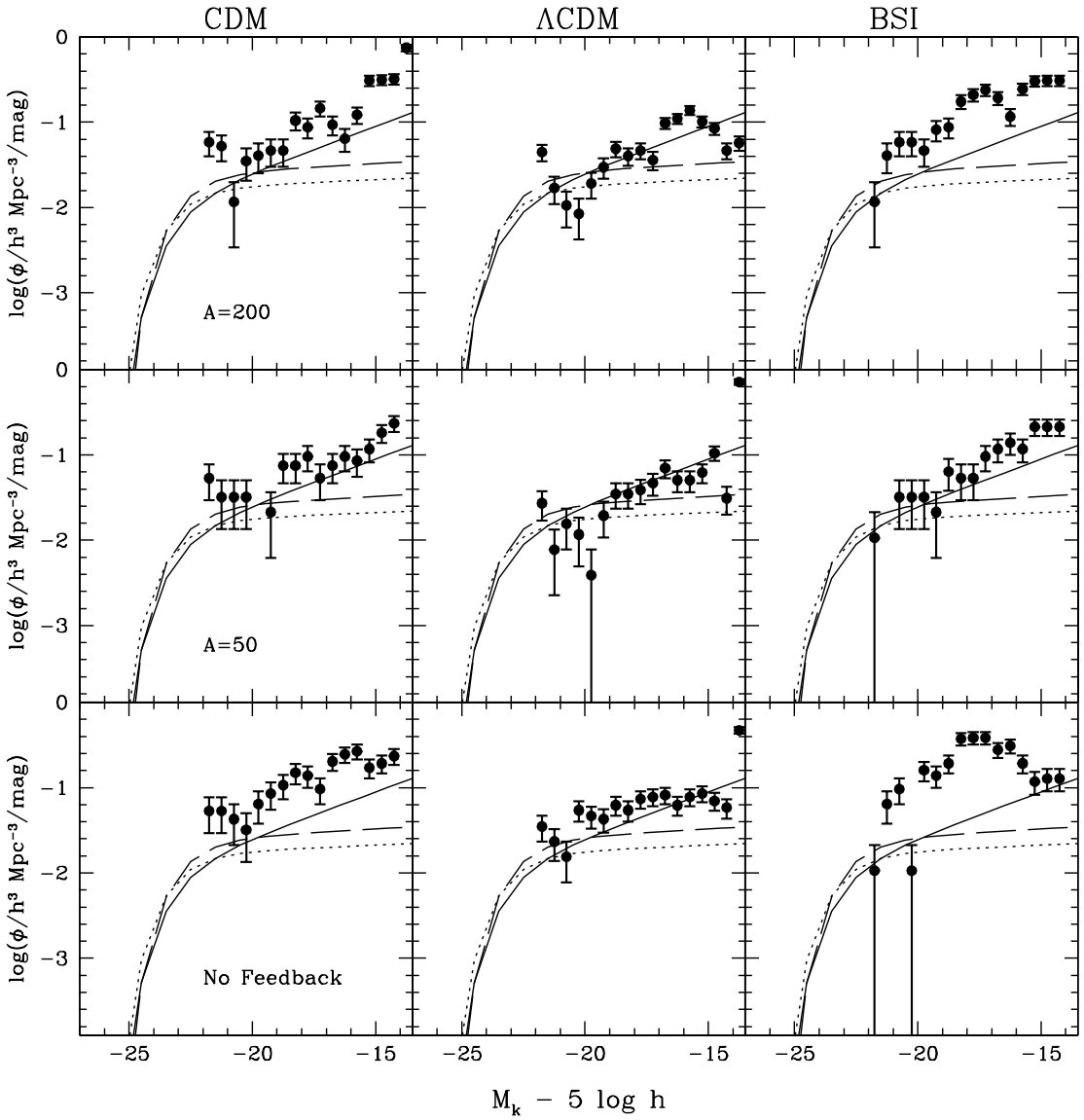


FIG. 12.—Same as Fig. 11, but for the *K* band. The solid line is the best-fitting Schechter function from Szokoly et al. (1998). The dotted line is the best fit to the LF obtained by Gardner et al. (1997). The dashed line corresponds to the best-fitting LF obtained by Glazebrook et al. (1995).

thick solid lines represent the average SFRs for halos of same virial mass, computed by means of the semianalytical model developed by Firmani & Avila-Reese (1998). The error bars represent the maximum and minimum SFR values at different redshifts for the 2000 Monte Carlo realizations of mass accretion histories for this halo. This semianalytical model of formation of disk galaxies includes a simplified hydrodynamical treatment of the gas and models the effects of supernovae on the cold gas clouds as an increase in their turbulent motion. This model differs from our picture of cloud evaporation, but it nonetheless provides an effective feedback mechanism. The scatter in the TF relation for these models is somewhat higher than the one we obtain in the simulations. However, the overall agreement between these semianalytical calculations and our simulations is remarkable. (See Firmani & Avila-Reese 1998 for further details.)

We have also estimated the LFs in *B* and *K* bands from the simulated galaxies. The relatively small volumes of our present simulations preclude a reliable estimate of the full LF in the different cosmological scenarios, since as explained earlier bright galaxies are undersampled or completely absent because of the lack of high-density regions. With this caveat in mind, we have compared the number density of faint objects with observations. The faint end of the LF is very much affected by supernova feedback. This is especially important for the less evolved BSI simulations, in which a high number density of faint objects is found. In all simulations, we systematically find steeper slopes for the *B*-band LFs than the estimates from the Stromlo-APM survey (Loveday et al. 1992), but they are compatible with recent estimates from the ESP (Zucca et al. 1997).

Despite possible uncertainties in the determination of the LF from our simulations, we can conclude that, with an adequately chosen value for the feedback parameter, our model of self-regulating star formation can reproduce the correct TF zero point and the right number density of objects, at least for the ΛCDM model. For the CDM simu-

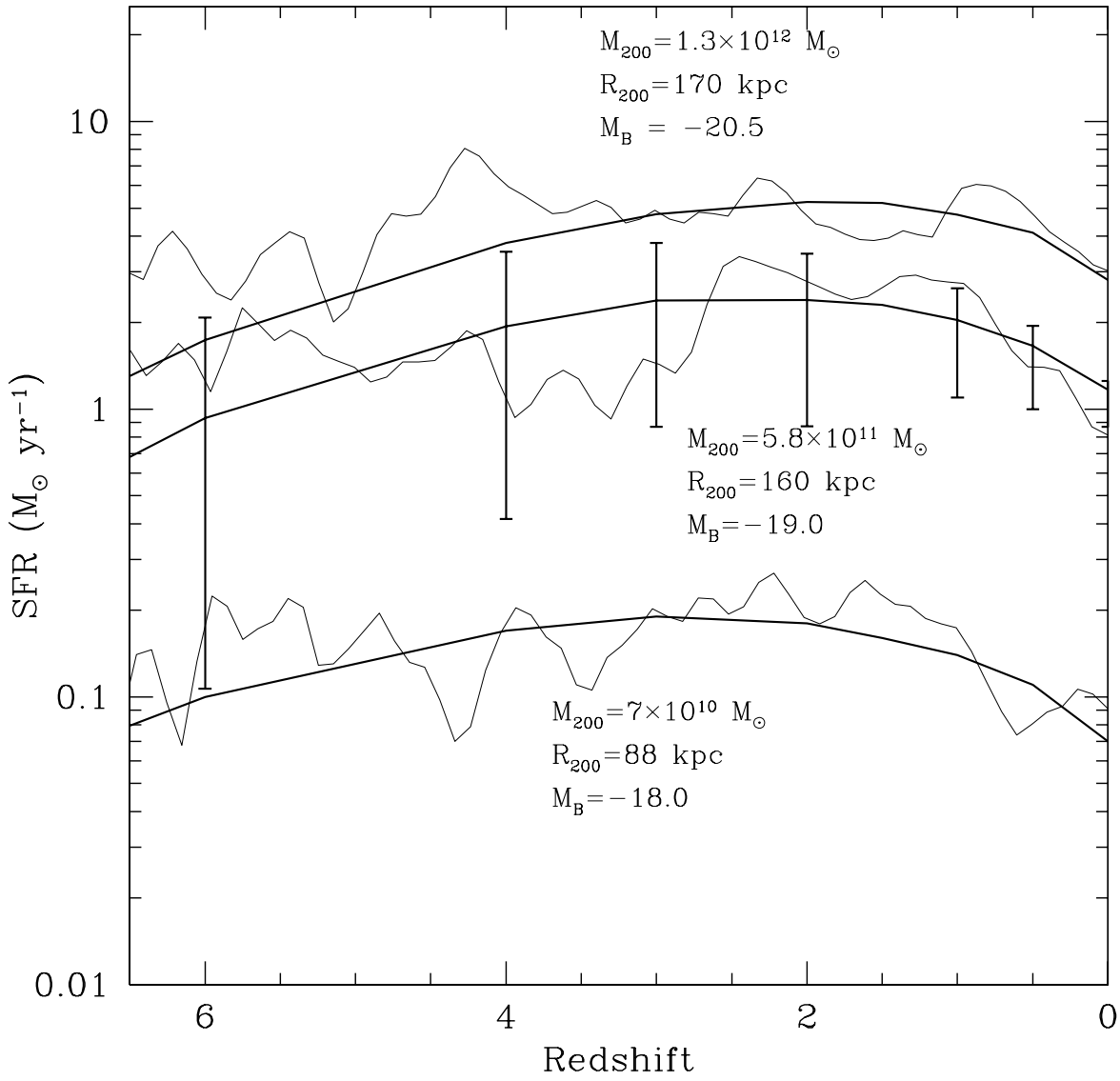


FIG. 13.—Comparison of the redshift evolution of the SFR for three different halos in one of our ΛCDM simulations (*thin solid lines*), with averaged predictions from semianalytical galaxy formation models (Firmani & Avila-Reese 1998). The error bars correspond to the maximum and minimum values of the SFR in the Monte Carlo realizations of mass accretion histories for the corresponding halo.

lations, halos tend to have lower luminosities for a given circular velocity, so the zero point of the TF relation is incompatible with observations, while for the BSI model, the low normalization of the spectrum produces far too many faint objects. The number of objects can be reduced by assuming a small value for the feedback parameter ($A = 50$), which means a large thermal reheating. In this case, the galaxies are fainter and the TF zero point is not compatible with the observed one.

We saw in § 5 that our results are fairly robust with respect to changes in numerical resolution and details of the galaxy-finding scheme. Doubling the resolution did not significantly affect the TF relation, although some individual galaxy colors were shifted. As resolution is further increased, we expect that some adjustment of parameters in our modeling of processes occurring below the limits of resolution will be required.

In recent work Steinmetz & Navarro (1998), using high-resolution smoothed particle hydrodynamics simulations with star formation in an SCDM model, have found results for the TF relation that are in fairly good agreement with the results shown in this paper for the same cosmological model. They conclude that the slope and scatter of the TF relation can be naturally explained in hierarchical models but the zero point depends strongly on the star formation algorithm and on the cosmological parameters chosen. We basically agree with the dependence of the zero point, but our results show that the slope, and to a lesser extent, the scatter, *do depend* on the modeling of feedback and on the cosmological model as well. Without feedback, our simulations predict a scatter and slope that are not compatible with the observed values.

An important goal of this work was to explain the observed low scatter in the TF relation without appealing to initial conditions. This low scatter arises self-consistently within our model: The hierarchical assembling of dark matter halos produces a tight correlation between total mass and circular velocity. One key feature that can be

inferred from our simulations is the presence of a nonlinear self-regulating mechanism involving the supply of cold gas for star formation. The self-regulating mechanisms of star formation produce a tight correlation between halo mass and star mass (see Fig. 4). They also cause halos of a given mass to exhibit rather similar star formation histories, despite different merging histories (see Elizondo et al. 1999 for more details). Therefore, the correlation between halo mass and stellar ages is tighter than one might otherwise have expected. The combination of all these processes produces a scatter in the TF relation that is compatible with the observed scatter.

Hence, the combined effects of self-regulating processes affecting star formation, including supernova feedback and gasdynamics, are all required for a proper understanding of the observed TF relation in the context of hierarchical models of galaxy formation.

We wish to thank Claudio Firmani and Vladimir Avila-Reese for helpful discussions and for providing us with comparisons from their semianalytical calculations. We would also like to thank Andrey Kravtsov for performing one of our CDM realizations using the ART code and computing the velocity profiles. This work has been partially supported by the DGICyT (Spain) under project number PB93-0252. R. K. gratefully acknowledges a fellowship of the DFG (Germany) during part of this work.

REFERENCES

Avila-Reese, V. 1998, Ph.D. thesis, Universidad Nacional Autónoma de México
Avila-Reese, V., Firmani, C., & Hernández, X. 1998, ApJ, 505, 37
Bruzual, G., & Charlot, S. 1993, ApJ, 405, 538
Cen, R., & Ostriker, J. P. 1992, ApJ, 399, 113
Cole, S., Aragón-Salamanca, A., Frenk, C. S., Navarro, J. F., & Zepf, S. E. 1994, MNRAS, 271, 781 (CAFNZ)
Cole, S., & Kaiser, N. 1989, MNRAS, 237, 1127
Colella, P., & Woodward, P. R. 1984, J. Comp. Phys., 54, 174
Courteau, S. 1997, AJ, 114, 2402
Eisenstein, D. J., & Loeb, A. 1996, ApJ, 459, 432
Elizondo, D. 1996, Ph.D. thesis, Universidad Autónoma de Madrid
Elizondo, D., Yepes, G., Kates, R., & Klypin, A. 1999, New Astron., in press
Evrard, A., Summers, F., & Davis, M. 1994, ApJ, 422, 11
Firmani, C., & Avila-Reese, V. 1998, ApJ, submitted (astro-ph/9803090)
Freeman, K. C. 1970, ApJ, 160, 811
Frenk, C. S., Baugh, C. M., Cole, S., & Lacey, C. 1997, ASP Conf. Ser. 117, Dark Matter 1996: Dark and Visible Matter in Galaxies and Cosmological Implications, ed. M. Persic & P. Salucci (San Francisco: ASP), 335
Gardner, J. P., Sharples, R. M., Frenk, C. S., & Carrasco, B. E. 1997, ApJ, 480, L99
Giroux, M., & Shapiro, P. 1986, ApJS, 102, 191
Glazebrook, K., Peacock, J. A., Miller, L., & Collins, C. A. 1995, MNRAS, 275, 65
Heyl, J. S., Cole, S., Frenk, C. S., & Navarro, J. F. 1995, MNRAS, 274, 755 (HCFN)
Kates, R., Müller, V., Gottlöber, S., Mücket, J. P., & Retzlaff, J. 1995, MNRAS, 277, 1254
Katz, N. 1992, ApJ, 391, 502
Katz, N., Hernquist, L., & Weinberg, D. H. 1992, ApJ, 399, 109
Katz, N., Weinberg, D. H., & Hernquist, L. 1996, ApJS, 105, 19
Kauffmann, G., White, S. D. M., & Guiderdoni, B. 1993, MNRAS, 264, 201 (KWG)
Kravtsov, A., Klypin, A., & Khokhlov, A. 1997, ApJS, 111, 73
Loveday, J., Peterson, B. A., Efstathiou G., & Maddox, S. J. 1992, ApJ, 390, 338
McKee, C. F., & Ostriker, J. P. 1977, ApJ, 218, 148
Navarro, J. F., & White, S. D. M. 1994, MNRAS, 267, 401
Persic, M., Salucci, P., & Stel, C. 1996, MNRAS, 281, 27
Petitjean, P., Mücket, J., & Kates, R. 1995, A&A, 295, L9
Pierce, M. J., & Tully, R. B. 1988, ApJ, 330, 579
———. 1992, ApJ, 387, 47
Somerville, R. C., & Primack, J. R. 1998, MNRAS, submitted (astro-ph/9802268)
Steinmetz, M., & Müller, E. 1994, A&A, 281, 97
Steinmetz, M., & Navarro, J. F. N. 1998, ApJ Lett., submitted (astro-ph/9808076)
Strauss, M. A., & Willick, J. A. 1995, Phys. Rep., 261, 271
Szokoly, G. P., Subbbarao, M. U., Connolly, A. J., & Mobasher, B. 1998, ApJ, 492, 452
Tully, R. B., & Fisher, J. R. 1977, A&A, 54, 661
Yepes, G., Kates, R., Khokhlov, A., & Klypin, A. 1997, MNRAS, 284, 235 (YK^3)
Yepes, G., Kates, R., Klypin, A., & Khokhlov, A. 1995, Proc. XVth Recontres des Moriond, Clustering in the Universe, ed. S. Maurogordato, C. Balowski, C. Tao, & J. Trán Thanh Ván (Gif-sur-Yvette: Editions Frontières), 403
Zucca, E., et al. 1997, A&A, 326, 477